Cross-correlation effect of ARAIM test statistic on false alarm risk

Eugene Bang, Carl Milner, Christophe Macabiau

Cross-Correlation Effect of ARAIM Test Statistic on False Alarm Risk

Eugene Bang[1], Carl Milner[1] and Christophe Macabiau[1]

[1] Department of Air Navigation Engineering, Ecole Nationale de l'Aviation Civile (ENAC), 7 Avenue Edouard Belin, 31055 Toulouse, France

Abstract

The requirement for ARAIM continuity risk due to the monitor false alarm has been outlined in earlier works for ARAIM development (WG-C 2016). However, the expected continuity risk comes from an underlying conservative assumption that the correlation between multiple monitors for fault detection is negligible. Thus, we investigate the effect of the cross-correlation across ARAIM solution separation tests on the monitor false alarm probability (P_{FA}) by presenting a higher fidelity methodology to evaluate the P_{FA} based on highly correlated fault detection tests. We carry out a preliminary assessment of ARAIM false alarm performance by using the proposed method. It was found that considering the cross-correlation amongst monitor test statistics reduces the predicted P_{FA} by up to approximately 50% of the predefined requirement (e.g., 10^{-6}) when triple satellite faults were considered. Despite such improvement, the baseline ARAIM implementation does not appear to be overly conservative.

Introduction

Single-frequency receiver autonomous integrity monitoring (RAIM) has been designed to mitigate Global Positioning System (GPS) integrity threats due to measurement faults (Lee 1986; Parkinson and Axelard 1998), and since the mid-1990s GPS with RAIM has been used as a navigation tool in safety-critical civil aviation applications (RTCA Special Committee 159 1991). With the modernization of GPS and the full deployment of new Global Navigation Satellite System (GNSS) constellations including the European Galileo, the Russian Global Orbiting Navigation Satellite System (GLONASS) and the Chinese BeiDou, an increased number of GNSS measurements are expected to be available. Such revolutionary improvements in the satellite constellations have recently drawn strong interest to expand the

use of RAIM to more stringent phases of aircraft navigation requiring vertical guidance (Blanch et al. 2015).

With this goal, the GPS Evolutionary Architecture Study (GEAS) outlined a new dual-frequency multi-constellation Advanced RAIM (ARAIM) concept and a corresponding user algorithm (FAA 2010; Blanch et al. 2007, Lee and McLaughlin 2007). Since the GEAS phase II report, there has been a substantial effort on development of a refined reference airborne algorithm, including fault detection and exclusion (FDE) methods, and potential ARAIM architectures in the Working Group C (WG-C) ARAIM Technical subgroup under the EU and U.S. Agreement on GPS-Galileo Cooperation (WG-C 2016). Two types of ARAIM service, Horizontal ARAIM (H-ARAIM) and Vertical ARAIM (V-ARAIM), were proposed. It has been concluded that the ARAIM service should be implemented progressively starting with the horizontal service H-ARAIM to support the near-term multi-constellation applications (WG-C 2016). Hence H-ARAIM is of primary interest to this work. The goal of H-ARAIM service is to assure navigation integrity for Required Navigation Performance (RNP) 0.1NM, which corresponds to the most stringent navigation requirement for H-ARAIM operations. V-ARAIM, a target operational service for ARAIM, is intended for Localizer Performance with Vertical guidance which guides an aircraft to 200-feet decision height (LPV-200) (WG-C 2016).

While many available measurements provide better accuracy and greater redundancy for integrity monitoring capability, the higher likelihood of satellite and constellation faults with newly deployed multi-constellations is likely to lead to a significant rise in ARAIM continuity risk. Therefore, Blanch et al. (2015) considered the monitor false alarm (FA) as the loss of continuity (LOC) source and designed the fault detection (FD) algorithm accordingly. Later works (Zhai et al. 2015, 2018; Bang et al. 2018) further investigated the impact of exploiting a lot more measurements on overall ARAIM continuity and demonstrated the need of an exclusion function by identifying all the sources of LOC and establishing a method to quantify their contributions to the continuity risk. Zhai et al. (2015, 2018) mainly examined the impact of the larger prior probabilities of GNSS faults and unscheduled satellite outages on the overall continuity risk. This is because the continuity risk due to monitor FA, one of the major causes of LOC, can be controlled by setting ARAIM FD threshold under each fault hypothesis such that the continuity and integrity requirement are both met (Blanch et al. 2015; Zhai et al. 2018).

The currently proposed ARAIM baseline algorithms (Blanch et al. 2015; Joerger et al. 2016) take a simple approach to modeling the expected FA rate. In the approach, the continuity budget for the FA event is evenly allocated between monitor statistics at each epoch, neglecting test statistic correlation. Thus, during the ARAIM development, it is crucial to predict and review the monitor performance with respect to integrity in the worst case, i.e., specific risk and continuity in an average risk sense (Zhai et al. 2015). Pervan et al. (2017), in the scope of the Ground Based Augmentation System (GBAS), addressed the autocorrelation of test statistics over time and the cross-correlation between monitors of different forms for the detection of the ionosphere. These results showed that higher FA rates could occur than predicted by the simplest partition of continuity risk between subsequent independent intervals by accounting for temporal correlation. However, to the authors' knowledge, no earlier work on the influence of the relationship amongst monitor statistics on the system performance have been carried out from the viewpoint of ARAIM. Therefore, we investigate the correlation between ARAIM test statistics. If the performance based on the cross-correlation assumption significantly exceeds its requirement, the resulting performance could be then used as a baseline to design more efficiently monitor thresholds to garner better real-time performance. Otherwise, there would be no need to modify the current ARAIM implementations due to the correlation.

We thus evaluate the false alarm probability (P_{FA}) of ARAIM monitoring by taking account of the cross-correlation between FD test statistics. We examine the single satellite fault, double and triple satellite faults, in which a better result is expected for the latter whereby the continuity budget is allocated to a large number of statistics thus increasing the thresholds. For this purpose, we first characterize the cross-correlation between solution separation test statistics for possible fault hypotheses at each satellite geometry. Since the tests are not entirely orthogonal in the parity domain (Sturza 1988), it is not easy to directly evaluate a Gaussian multivariate distribution with a singular covariance structure between the correlated tests. Hence, we need to recognize independent tests to take credit for those test results efficiently. We identify a more straightforward multivariate normal distribution with reduced size full rank covariance matrix between the orthogonal tests than for the full ensemble of tests. Next, we numerically determine the P_{FA} based on the reduced multivariable Gaussian distribution and compare it with the predefined requirement (WG-C 2016). By doing this, we can reduce the complexity of the computation of average continuity risk whilst more appropriately matching the real performance. The mechanisms here require substantial numerical computation load

and are not intended for real-time implementation. However, continuity may be assessed offline in an average sense. Therefore, the results could still be employed to modify the continuity allocation to real-time detection thresholds, if necessary. In comparison to results shown in Bang et al. (2019) and Pervan et al. (2017), it is evident that cross-correlation and temporal correlations have opposing effects. A lower FA rate can be achieved than the predefined requirement by considering the cross-correlation between test statistics. Thus, we examine how much continuity margin can be achieved by considering the cross-correlations between ARAIM monitor test statistics.

The next section introduces the overall ARAIM continuity risk concept proposed in the literature to clarify the continuity risk requirement for ARAIM operations and underlying assumptions used. In the following sections, the least-squares estimation of states of interest and the current ARAIM FD algorithm are reviewed to define the ARAIM solution separation detection test. A methodology we applied for the evaluation of the P_{FA} of ARAIM FD test is detailed next. With the method fully described, example P_{FA} assessments are carried out using simplified cases and the methodology. The parity-space representation (Joerger and Pervan 2016) for the ARAIM FD is also employed to understand the proposed method better. We then present the resulting false alarm performance given simulation conditions, including different combinations of satellite faults, discuss the effect of the test correlation on the continuity performance, and concludes with remarks on future work.

Continuity risk allocation for ARAIM monitor false alarm

This section outlines the continuity risk allocation to ARAIM FA event, which involves the quantification of the impact of GNSS fault on the overall continuity risk for ARAIM. The continuity requirement for ARAIM operation is first described, and an example continuity allocation for this study is then explained. Next, a bound on the P_{FA} is defined. The assumption and the bound in this section will be used in the remainder of the paper.

Table 1 lists integrity and continuity requirements (ICAO 2014) for different types of operations, which ARAIM is intended to support: RNP 0.1 and LPV-200. These are expected to be the most stringent level of navigation service that H- and V-ARAIM respectively target (WG-C 2016). Horizontal operations have more straightforward requirements and can be supported with today's RAIM; hence the first form of ARAIM implementation, which is a

natural evolution of RAIM, will be H-ARAIM (WG-C 2016), and RNP 0.1 will be considered in this work.

Table 1 Navigation Requirement for RNP 0.1 and LPV-200

Type of Service	Alert Limit	Integrity risk requirement	Continuity risk requirement
RNP 0.1	185 m (HAL)	10^{-7} per hour	10^{-4} per hour to 10^{-8} per hour
LPV-200	40 m (HAL) / 35 m (VAL)	10^{-7} per approach	10^{-4} per hour to 10^{-8} per hour

According to International Civil Aviation Organization (ICAO) (ICAO 2014), the continuity of service of a system is defined as the capability of the system to perform its function without unscheduled interruptions during the intended operation and it should be understood in an average sense. ICAO (2014) specifies the requirement on an hourly basis in a certain range rather than a single value, as shown in Table 1. This is because the continuity requirement is dependent upon several factors, including the traffic density and complexity of airspace around an airport and the availability of alternative navigation aids. Recent works (Zhai et al. 2016, 2018) on ARAIM continuity risk evaluation set the intermediate value of 10^{-6} per hour, which accounts for a case of high air traffic density and airspace complexity, as the total continuity risk requirement for H-ARAIM performance simulation. Those works also identified four different source events which lead to unscheduled mission interruptions (i.e., LOC), and comprehensively assessed the average risk of LOC (P_{LOC}) by quantifying the impact of each event on P_{LOC} under several assumptions. We stay consistent with the previously proposed allocation of the continuity risk requirement and categorization of those causes of LOC, which includes monitor FA event, FD and unscheduled satellite outages (Zhai et al. 2016).

Unlike the previous studies, the present work aims to analyze the impact of cross-correlation between ARAIM monitors on the monitor false alarm rate and examine the gap between the requirement and the actual P_{FA}. Therefore, this work first divides P_{LOC} into two main groups: LOC due to false alarm (i.e., P_{FA}) and all other contributions (P_{others}), as shown

in

$$P_{LOC} = P_{FA} + P_{others} \quad (1)$$

More details on other contributions except for those to P_{FA} can be found in Zhai et al. (2016, 2018).

Next, we will assume that the contribution of the navigation interruptions due to other events on P_{LOC} is negligible, i.e., $P_{others} = 0$, and we thus consider the FA event as the cause of LOC. Note that this assumption is certainly not realistic because of the impact of FD on P_{LOC} could be significant (Zhai et al. 2016, 2018). However, we apply the upper bound of 10^{-6} to P_{FA} as an example allocation.

In the current multiple-hypothesis based ARAIM FD mechanism (Blanch et al. 2015; Joerger and Pervan 2016), all possible fault hypotheses are investigated to identify and remove a potential satellite fault mode. Therefore, P_{FA} is defined as:

$$P_{FA} = P(|q_1| \geq T_1 \cup |q_2| \geq T_2 \cup \cdots \cup |q_i| \geq T_i \cdots \cup |q_h| \geq T_h | H_0) P_{H_0} \quad (2)$$

where i is the index denoting a set of mutually exclusive and collectively exhaustive hypotheses and h is the number of the hypotheses (i.e., $i = 0,1,\cdots,h$). H_0 represents the fault-free hypothesis and the remaining hypotheses, H_i, for $i = 1,\cdots,h$ include single satellite fault modes and multiple satellite fault modes. P_{H_0} is a prior-probability of the fault-free condition and is set as one. $q_i$is the i^{th} FD test statistic under H_0 and T_i is the corresponding detection threshold. If any of the test statistics exceed the given threshold, an alarm will be triggered. The continuity risk requirement for the FA event is then allocated to each of the tests to determine the corresponding test threshold in a conservative way, which will be detailed in the next section.

ARAIM Solution separation threshold test

This section briefly addresses current ARAIM FD method based on the solution separation

threshold test (WG-C 2016; Blanch et al. 2015) to determine the P_{FA}. Although ARAIM FDE algorithms have been proposed in the literature (Blanch et al. 2014, 2015; Joerger and Pervan 2016; Milner et al. 2017), the fault exclusion is not covered here. Notations in this section are used in the remainder to describe the P_{FA} evaluation methodology.

Let us assume that we have *h* different fault hypotheses. For each hypothesis from 1 to *h*, the solution separation, $\Delta\hat{\boldsymbol{x}}_i$, is defined as the difference between the subset solution, $\hat{\boldsymbol{x}}_i$, and the all-in-view solution, $\hat{\boldsymbol{x}}_0$:

$$\Delta\hat{\boldsymbol{x}}_i = \hat{\boldsymbol{x}}_i - \hat{\boldsymbol{x}}_0 = (\mathbf{S}_i - \mathbf{S}_0)\mathbf{y} \qquad \text{for } i = 1,2,\cdots,h \tag{3}$$

where $\mathbf{y}$ is a measurement vector and $\hat{\boldsymbol{x}}_i$ indicates the subset solution which is obtained using all satellites except the faulty satellites under the hypothesis, H_i, and $\hat{x}_0$ designates the full-set estimate based on all-in-view satellites. The matrix $\mathbf{S}$ is a projection matrix from the measurement domain to the position domain and $\mathbf{S_i}$ for each hypothesis H_i is computed by setting the weight of faulty measurements under H_i as zero in the weighted least-squares estimation (Blanch et al. 2015). Next, let the index k be the index used to represent a state of interest, e.g., the horizontal position coordinate for H-ARAIM. The standard deviation of the solution separation, $\sigma_{\Delta\hat{x}_i,k}$, for the *k*-th state is then computed:

$$\sigma_{\Delta\hat{x}_{i,k}} = \sqrt{\boldsymbol{u}_k^T\left((\boldsymbol{S}_i - \boldsymbol{S}_0)\mathbf{C}(\boldsymbol{S}_i - \boldsymbol{S}_0)^T\right)\boldsymbol{u}_k} \tag{4}$$

where $\boldsymbol{u}_k$ is a unit vector whose *k*-th component is '1' and all other entries are '0' and $\mathbf{C}$ is the covariance matrix of the measurement vector $\mathbf{y}$. More details on the determination of the matrices above and the weighted least-squares method can be found in Blanch et al. (2015).

The FD threshold for fault mode i and state index k is then defined by

$$T_{\Delta\hat{x}_{i,k}} = K_{fa,k}\sigma_{\Delta\hat{x}_i,k} \tag{5}$$

The factor $K_{fa,k}$ is determined as follows:

$$K_{fa,k} = Q^{-1}\left(\frac{P_{FA,REQ,k}}{2h}\right) \tag{6}$$

$Q^{-1}(\cdot)$ denotes the inverse tail probability distribution of the unit normal distribution and $P_{FA,REQ,k}$ is the continuity requirement for the k-th state, and it is evenly allocated into fault hypotheses. All the test statistics in (3) are evaluated and then compared to corresponding thresholds for all hypotheses. If *any* of the statistics exceed the associated threshold, the fault that makes the test fail is detected. In other words, the fault is detected if the condition in holds:

$$\left|\Delta\hat{x}_{i,k}\right| = \left|\hat{x}_{i,k} - \hat{x}_{0,k}\right| \geq T_{\Delta\hat{x}_{i,k}} \text{ for any } i, \text{ and } i = 1,2,\cdots,h \tag{7}$$

Note that we use the solution separation test statistic, but other, loosely equivalent metrics would produce similar results if not exactly equivalent results (Kelly 1998; Young and McGraw 2003). Based on the FD method explained above, the next section gives some descriptions of P_{FA} of the ARAIM solution separation test.

Methodology

This section outlines a methodology for the P_{FA} evaluation, which is in line with the solution separation threshold test. The P_{FA} is briefly reviewed, followed by a description of cross-correlation across ARAIM test statistics. Next, the P_{FA} evaluation method for ARAIM solution separation monitor is explained.

Cross correlation across test statistics

Let us assume we have h fault hypotheses at a specific satellite geometry. Also, we consider only a single state, x, to describe the method instead of the full state vector, **x**, defined in the previous section. Thus, the state index k in (4) is no longer used in this section. The P_{FA} in (2) can then be given as the following joint probability:

$$P_{FA} = P\left(|\Delta\hat{x}_1| \geq T_{\Delta\hat{x}_1} \cup |\Delta\hat{x}_2| \geq T_{\Delta\hat{x}_2} \cup \cdots \cup |\Delta\hat{x}_h| \geq T_{\Delta\hat{x}_h} | H_0\right) \tag{8}$$

Equation (8) can be expressed as:

$$P_{FA} = 1 - P\left(|\Delta\hat{x}_1| < T_{\Delta\hat{x}_1} \cap |\Delta\hat{x}_2| < T_{\Delta\hat{x}_2} \cap \cdots \cap |\Delta\hat{x}_h| < T_{\Delta\hat{x}_h} | H_0\right) \quad (9)$$

$$= 1 - \mathrm{P}\left[\bigcap_{i=1}^{h}\left(-T_{\Delta\hat{x}_i} < \Delta\hat{x}_i < T_{\Delta\hat{x}_i}\right) | H_0\right]$$

The multivariate Gaussian distribution needs to be evaluated over h constraints based on solution separation thresholds (see (5)) to calculate the P_{FA}. The last joint probability in (9) can be rewritten as:

$$\mathrm{P}\left[\bigcap_{i=1}^{h}\left(-T_{\Delta\hat{x}_i} < \Delta\hat{x}_i < T_{\Delta\hat{x}_i}\right) | H_0\right] \quad (10)$$

$$= \frac{(2\pi)^{-h/2}}{\sqrt{|\mathbf{\Sigma}|}} \int_{-T_{\Delta\hat{x}_1}}^{T_{\Delta\hat{x}_1}} \cdots \int_{-T_{\Delta\hat{x}_h}}^{T_{\Delta\hat{x}_h}} \exp\left[-\frac{1}{2}(\mathbf{\Delta X}^T \mathbf{\Sigma}^{-1} \mathbf{\Delta X})\right] d\Delta\hat{x}_h \cdots d\Delta\hat{x}_1$$

where $\mathbf{\Delta X} = [\Delta\hat{x}_1, \Delta\hat{x}_2, \cdots, \Delta\hat{x}_h]^T$ follows a h-variate normal distribution with zero mean and covariance $\mathbf{\Sigma}$, i.e., $\mathbf{\Delta X} \sim N_h(\mathbf{0}, \mathbf{\Sigma})$. For the evaluation of the probability, we first define the covariance matrix amongst solution separations, $\mathbf{\Sigma}$, in (10):

$$\mathbf{\Sigma}_{\mathrm{ij}} = E\left[\Delta\hat{x}_i \Delta\hat{x}_j^T\right] = (\boldsymbol{S}_i - \boldsymbol{S}_0)\mathbf{C}\left(\boldsymbol{S}_j - \boldsymbol{S}_0\right)^T \qquad i, j = 1,2,\cdots,h \quad (11)$$

where $\mathbf{C}$ and $\boldsymbol{S}$ are respectively defined in (3) and (4). Let us consider two constellations, e.g., GPS and Galileo. Since the number of states in our least-squares estimation is five, i.e., three position coordinates and two clock biases for the two constellations, the covariance matrix is at most of rank h-5., which means we will only be able to extract h-5 orthogonal tests. Therefore, the covariance matrix, $\mathbf{\Sigma}$, will be singular in our problem. In order to handle the singular covariance matrix, we propose a computation method which fits such singular multivariate distribution to assess rigorously the P_{FA}.

Evaluation of false alarm probability

As discussed in the previous section, our test statistic domain has at most h-5 dimensions. Thus,

for a given covariance matrix $\mathbf{\Sigma}$ based on test statistics, rank ($\mathbf{\Sigma}$) = $r < h$ and its inverse does not exist, (9) would not therefore be well-defined. In addition, the integral for the multivariate Gaussian distribution has no general analytical solution, so it must be evaluated numerically. Thus, a transformation which is expressed as an h by r matrix, $\mathbf{Q}$, was identified to define a change of variable $\mathbf{\Delta X} = \mathbf{Qy} = \mathbf{Q}[y_1, y_2, \cdots, y_r]^T$ using a method described by (Genz and Kwong (2000) so that the evaluation of the inverse of the covariance matrix is not required to integrate the distribution after the transformation. The transformation matrix $\mathbf{Q}$ can be obtained by the generalized Cholesky factorization (Healy 1968; Gene and Charles 2013) such that even the singular covariance matrix can be factored as $\mathbf{\Sigma} = \mathbf{QQ}^{\mathrm{T}}$, where $\mathbf{Q}$ is a lower triangular and has some zero entries on the main diagonal. After performing the change of variable, $\mathbf{\Delta X} = \mathbf{Qy}$, the probability in (10) can be reduced in the following form:

$$\frac{(2\pi)^{-\frac{h}{2}}}{\sqrt{|\mathbf{\Sigma}|}} \int_{-T_{\Delta\hat{x}_1}}^{T_{\Delta\hat{x}_1}} \cdots \int_{-T_{\Delta\hat{x}_h}}^{T_{\Delta\hat{x}_h}} \exp\left[-\frac{1}{2}(\mathbf{\Delta X}^T \mathbf{\Sigma}^{-1} \mathbf{\Delta X})\right] d\Delta\hat{x}_h \cdots d\Delta\hat{x}_1 \tag{12}$$

$$= (2\pi)^{-r/2} \int_{\mathbf{-T<Qy<T}} \exp\left[-\frac{1}{2}(\mathbf{y}^T\mathbf{y})\right] d\mathbf{y}$$

where $\mathbf{T} = \left[T_{\Delta\hat{x}_1}, T_{\Delta\hat{x}_2}, \cdots, T_{\Delta\hat{x}_h}\right]^T$ and the integration region is still defined by h inequality constraints, $-\mathbf{T} < \mathbf{Qy} < \mathbf{T}$. However, the matrix $\mathbf{Q}$ has the lower triangular form where entries $q_{ij} = 0$ for all $j > r$ and the constraints on $\mathbf{y} = [y_1, y_2, \cdots, y_r]^{\boldsymbol{T}}$, thus, could contain multiple conditions for each y_i for $i = 1,2, \cdots, r$.

The set of h constraints on $\mathbf{y}$ can be reorganized by simple algebraic manipulations to generate a single constraint on each y_i for $i = 1,2, \cdots, r$ (see Appendix). Thus, a resulting integration with fewer dimension r (i.e., $< h$) can be reformulated as:

$$(2\pi)^{-\frac{r}{2}} \int_{\mathbf{-T<Qy<T}} \exp\left[-\frac{1}{2}(\mathbf{y}^T\mathbf{y})\right] d\mathbf{y} \tag{13}$$

$$= (2\pi)^{-r/2} \int_{L_1}^{U_1} \exp\left(-\frac{y_1^2}{2}\right) \int_{L_2(y_1)}^{U_2(y_1)} \exp\left(-\frac{y_2^2}{2}\right) \cdots \int_{L_r(y_1, y_2, \cdots, y_{r-1})}^{U_r(y_1, y_2, \cdots, y_{r-1})} \exp\left(-\frac{y_r^2}{2}\right) d\mathbf{y}$$

where L_1 and U_1 are lower and upper bounds for the transformed y_1, respectively. Also, the lower and upper bounds for i-th integration, for $i = 2, \cdots, \mathrm{r}$, are respectively defined as a

function of different variables from the *i*-th variable, y_i, that is, $L_i = f(y_1, y_{2,} \cdots, y_{i-1})$. More details on the development of the integration form and the reorganization of the constraints are described in the Appendix.

Both the integrands within the multiple integrations and the integration bounds can be simplified by exploiting a couple of simple algebraic transformations, such that (13) is suitable for standard numerical integration methods. After the conversion, the final form of (13) can be reduced:

$$(\bar{U}_1 - \bar{L}_1) \int_0^1 \left(\bar{U}_2(u_1) - \bar{L}_2(u_1)\right) \cdots \int_0^1 \left(\bar{U}_r(u_1, \cdots, u_{r-1}) - \bar{L}_r(u_1, \cdots, u_{r-1})\right) \int_0^1 d\boldsymbol{u} \quad (14)$$

and P_{FA} can be calculated as follows:

$$1 - (\bar{U}_1 - \bar{L}_1) \int_0^1 \left(\bar{U}_2(u_1) - \bar{L}_2(u_1)\right) \cdots \int_0^1 \left(\bar{U}_r(u_1, \cdots, u_{r-1}) - \bar{L}_r(u_1, \cdots, u_{r-1})\right) \int_0^1 d\boldsymbol{u} \quad (15)$$

Here the new vector **u** and the corresponding upper ($\bar{U}$) and lower ($\bar{L}$) limits can be expressed as a function of **y**. More details on the transformations and the relationship between **u** and **y** are described in the Appendix. The evaluation of the multiple integrations includes numerical calculations based on the Monte Carlo method, and the results of the numerical computation will be given in the next section.

Simulation results

To examine the actual P_{FA} redefined in the previous section, we conduct P_{FA} simulations based on the proposed method. First, some simple examples, which are called 'canonical example' (Eugene et al. 2018; Joerger and Pervan 2016) are addressed, showing how the proposed method works. Second, an analysis based on a combination of GPS and Galileo constellation is carried out using the proposed method. The baseline simulation conditions which are specified in some earlier works (WG-C 2016; Blanch et al. 2015) are applied to the analysis, and those conditions will also be shown in the following sections.

Canonical examples

Three one-dimensional canonical examples were first tested to demonstrate the validity of the evaluation method for the P_{FA}. In these cases, a single scalar state, x, and simple measurement models in Table 2 are assumed. The first example considers two satellites from a single constellation and two single fault modes corresponding to each measurement. As the next steps, two additional 1-D cases were examined: one with three 1-D measurements and three single fault modes and the other one with four measurements and four single failures. Also, unit variances for all measurement noises are assumed.

Table 2 Measurement models for three canonical examples and the continuity budget

Measurement model	Case	Observation matrix ($\mathbf{G}$)	Measurement noise ($\boldsymbol{\varepsilon}$)	Continuity budget ($P_{FA,REQ}$)
$\mathbf{y} = \mathbf{G}x + \boldsymbol{\varepsilon}$	1	$[1,1]^{\mathrm{T}}$	$N(0, \boldsymbol{I}_2)$	10^{-1}
	2	$[1,1,1]^{\mathrm{T}}$	$N(0, \boldsymbol{I}_3)$	10^{-1}
	3	$[1,1,1,1]^{\mathrm{T}}$	$N(0, \boldsymbol{I}_4)$	10^{-1}

As mentioned earlier, the numerical integration for the probability computation was performed using the Monte Carlo method. For three canonical examples, Monte Carlo iterations of 10^4 were tried to evaluate the probability. Since the likelihood could be differently assessed every trial due to the numerical integration error, the probability calculation is conducted 150 times for each case. Also, the median value of the resulting probabilities is taken to obtain a robust estimate against outliers due to the numerical approach. More discussions on the uncertainty of the numerical approach will be given in the next section. Table 3 shows results obtained by applying geometries and measurement models in Table 2.

Table 3 Simple single constellation based canonical example P_{FA}

Case	Fault mode	P_{FA} (median)
1	Single satellite fault	0.0500
2	Single satellite fault	0.0842
3	Single satellite fault	0.0890

As seen in Table 3, the P_{FA} obtained by accounting for correlation between tests is decreased (i.e., by 50% compared to the requirement of 10^{-1}) in the first case. In this case, as the rank of the observation matrix is one, with two perfectly correlated tests, such improvement can be expected. Since the number of independent tests is less than the number of the full combination of tests, the actual P_{FA} tends to be less than a given requirement. Like the first example, the number of independent tests in the second case can be expected to be two i.e., the number of measurements minus the number of states of interest. Despite the rank of two, the computed probability of approximately 0.084 is different from the simple guess which is two-thirds of the total budget of 10^{-1} (i.e., about 0.067). The gap between the expected probability and the computed one can be explained by showing the integration region after the transformation over which the P_{FA} is computed. In particular, the new random vector, $\mathbf{y}$, after the transformation has the covariance matrix, $\mathbf{I}_{2\times2}$, as mentioned in the previous section. Also, the parity vector (Sturza 1988; Jeorger et al. 2014) associated with the second example has the same covariance matrix, hence the integration region after the transformation can be expressed in the parity domain.

Let us assume we have n measurements and m states to be estimated. The $n-m$ dimensional parity vector, $\mathbf{p}$, is defined by the transformation from the measurement space to the parity space as expressed in (16)

$$\mathbf{p} = \mathbf{P}\mathbf{y} \tag{16}$$

The $(n-m)\times n$ parity matrix $\mathbf{P}$ whose row vectors are the orthonormal basis for the parity space, or left null space of $\mathbf{G}$, is defined such that

$$\mathbf{P}\mathbf{P}^{\mathbf{T}} = \mathbf{I}_{\boldsymbol{n-m}} \text{ and } \mathbf{P}\mathbf{G} = \mathbf{0}_{(\boldsymbol{n-m})\times\boldsymbol{m}} \tag{17}$$

Since the parity vector provides direct observation of the impact of the measurement fault (Sturza 1988), we employ the parity space representation in this section to visualize the fault detection mechanism. For the configuration of the second example, we have $n = 3$ and $m = 1$

and thus two-dimensional parity space, as shown in Figure 1. Black lines are three fault mode lines on which the mean parity vector exists as the magnitude of the fault (Jeorger et al. 2014) and blue lines correspond to the normalized solution separation detection thresholds, represented as T, for their corresponding fault modes. Those normalized detection thresholds are expressed as $T_{\Delta\hat{x}_i}/\sigma_{\Delta\hat{x}_i} = K_{fa,i}$ for $i = 1,2,3$ instead of those in (5). More details on the parity vector and the corresponding parity space can be found in earlier works (Sturza 1988; Jeorger et al. 2014). If we consider the even continuity allocation, the detection boundaries are a hexagon, as shown in the figure, and no detection region is defined as the inner part of the hexagon (Jeorger et al. 2014).

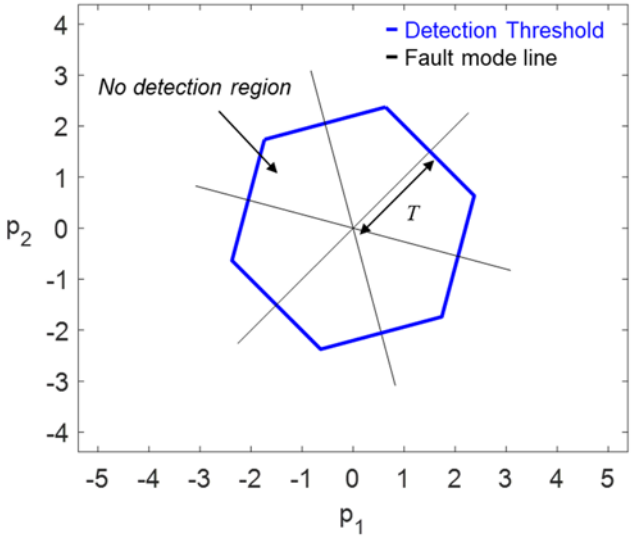

Fig. 1 Fault detection boundaries for the solution separations in the parity space

Next, to show how the detection boundaries for the random vector **y** form during the transformation, we first consider the lower and the upper bounds in (13) for the canonical example as follows:

$$\begin{bmatrix} L_1 \\ L_2 \\ L_3 \end{bmatrix} \leq \mathbf{Qy} = \begin{bmatrix} 1 & 0 \\ q_{2,1} & 1 \\ q_{3,1} & 1 \end{bmatrix} \begin{bmatrix} y_1 \\ y_2 \end{bmatrix} \leq \begin{bmatrix} U_1 \\ U_2 \\ U_3 \end{bmatrix} \tag{18}$$

where two constraints on y_2 and associated lower bounds (i.e., L_2 and L_3) and upper bounds (i.e., U_2 and U_3) are functions of y_1 and represent lines in the parity space. More specifically,

those two inequalities have the form:

$$L_2 - q_{2,1}y_1 \leq y_2 \leq U_2 - q_{2,1}y_1 \text{ and } L_3 - q_{3,1}y_1 \leq y_2 \leq U_3 - q_{3,1}y_1 \qquad (19)$$

As for the lower triangular form of the resulting matrix, **Q**, in (18), more details can be found in the Appendix. Figure 2 shows bounds in (19) in the parity space.

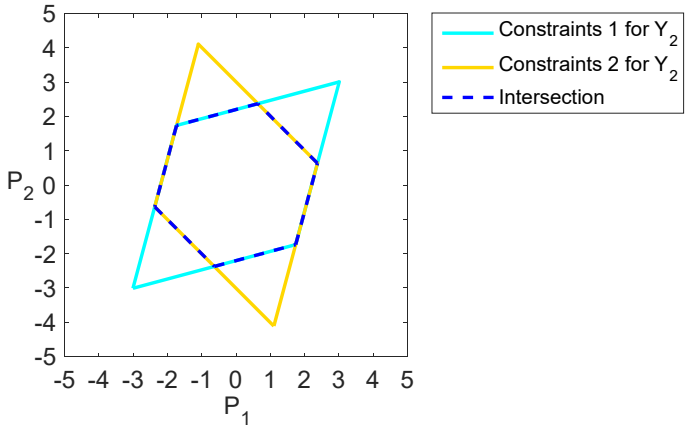

Fig. 2 Detection boundaries (yellow and light blue parallelograms) defined by two constraints on the new random variable (y_2) after the transformation in the parity space. A single constraint on y_2, the intersection of two regions, is the same as the detection bounds based on the parity vector (dotted blue hexagon)

In Figure 2, light blue and yellow lines respectively indicate boundaries from the first and the second inequalities defining y_2 in (19) given the limits for y_1 in (18). A single constraint on y_2 can be determined by identifying the intersection of two regions surrounded by those boundaries. As a result, detection boundaries based on y_1 and y_2 form the blue dotted hexagon in the space that is the same detection region defined by the parity vector (see Figure 1). Since the P_{FA} is the probability that the vector **y** lies outside the hexagon area, the evaluation using the proposed method should be equivalent to that based on the joint probability density of the parity vector.

For better understanding, we compare the pure guess based on the matrix rank and the actual calculation in Figure 3. In the figure, the red square based on the simple rank of two,

the guess, leads to a smaller probability (i.e., two-thirds of $P_{FA,REQ}=10^{-1}$) than the computed one in Table 3. However, in reality, the computed probability which accounts for the more complex boundaries, in three directions instead of two, lies between the full allocation (i.e., 10^{-1}) and the simple guess, as shown in Table 3. Also, since areas of the hexagon and the square are determined by the normalized detection thresholds for the given requirement (i.e., K_{fa} factor in (6)), it can be proven easily by the simple geometry that the area of the square is greater than that of the hexagon when those polygons have the same width.

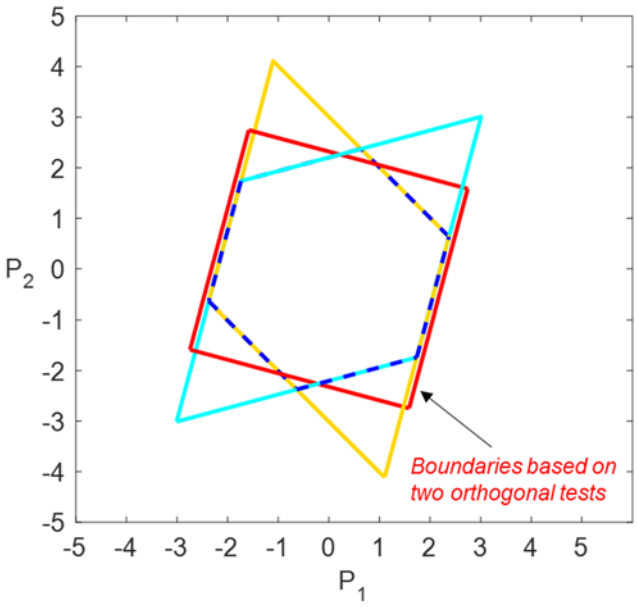

Fig. 3 Comparison of detection bounds by two independent tests, initial guess (red square), and that based on the transformation (blue dotted hexagon)

We also investigated another example by adding a satellite in the same direction. In the third case, the vector **y** has the covariance matrix, $\mathbf{I}_{3\times3}$, and the corresponding parity space is three-dimensional. Relevant lower and upper bounds after the transformation are shown in

$$\begin{bmatrix} L_1 \\ L_2 \\ L_3 \\ L_4 \end{bmatrix} \leq \mathbf{Qy} = \begin{bmatrix} 1 & 0 & 0 \\ q_{2,1} & 1 & 0 \\ q_{3,1} & q_{3,2} & 1 \\ q_{4,1} & q_{4,2} & 1 \end{bmatrix} \begin{bmatrix} y_1 \\ y_2 \\ y_3 \end{bmatrix} \leq \begin{bmatrix} U_1 \\ U_2 \\ U_3 \\ U_4 \end{bmatrix} \tag{20}$$

In this case, we have four constraints on the vector $\mathbf{y} = [y_1, y_2, y_3]$, and L and U respectively

indicate the corresponding lower and upper bounds obtained by the transformation. Like the second case, the upper and lower bounds on y_2 are all functions of y_1, and those bounds form lines in the three-dimensional parity space. Also, bounds on y_3 are identified by both y_1 and y_2, and thus those bounds become surfaces in the parity space. The no-detection region, which is defined by the combination of the given constraints, is shown in Figure 4.

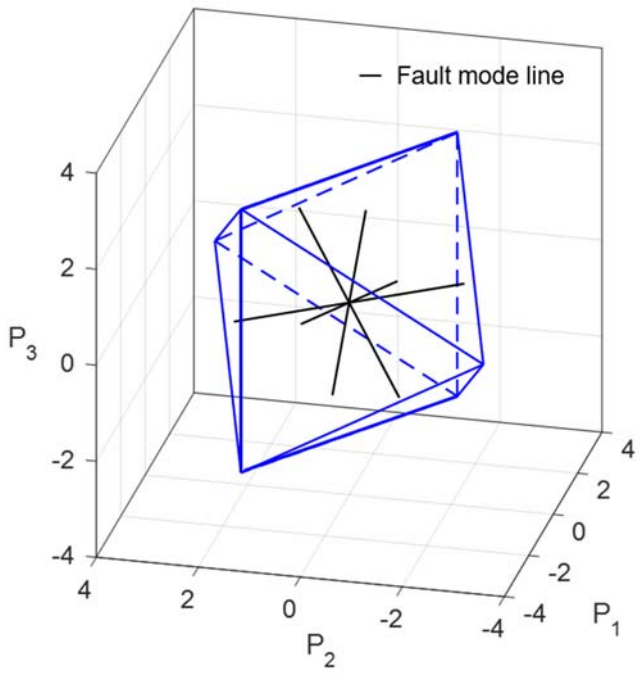

Fig. 4 No-detection zone for y_1, y_2 and y_3 obtained from the transformation in the three-dimensional parity space (blue octahedron). No-detection region based on four fault lines (black lines) is the same as the region based on the transformation in the parity domain

In Figure 4, black lines are fault mode lines formed by the parity vector, and the blue octahedron designates the detection bounds which are determined by the constraints on y_1, y_2 and y_3. It was checked that those detection bounds are the same as those based on fault lines and the corresponding thresholds in the parity space (Joerger and Pervan 2016). Like the previous two-dimensional parity space case, a higher probability (see Table 3) was observed than the initial guess (i.e., three-fourths of the requirement) where the detection boundaries look like a cube in the parity space. For the sake of simplicity, the cube is not represented in Figure 4.

Preliminary assessment of P_{FA} for solution separation ARAIM

We have examined some simple examples to evaluate the P_{FA}. In this section, to further extend the understanding of the impact of the correlation across ARAIM test statistics on the false alarm performance, four simulations were conducted assuming different fault modes: single and double satellite failures, a combination of a single and double satellite faults and triple faults. Underlying vital assumptions and parameters specified in WG-C (2016) are used to perform the simulations. The dual-frequency 24 GPS/Galileo baseline constellation with formal parameters (WG-C 2016) is used and the results were assessed for H- ARAIM operation. The false alarm requirement is set to be 10^{-6}, and 10^8 Monte Carlo trials are carried out to estimate the P_{FA} at each user location and each satellite geometry. Table 4 shows some key simulation parameters.

Table 4 P_{FA} simulation parameters

Parameter	Description	Parameter	Description
Constellation	24 GPS + 24 GAL	σ_{URA}	GPS/GAL: 2.5m
$P_{FA,REQ}$	10^{-6}	Monte Carlo trials	10^8
Mask Angle	5 deg.	User grid formation	10 deg. by 10 deg.
Simulation Time Step	10 mins	Simulation Duration	48 hours

Figure 5 shows an example time series of the P_{FA} obtained at a specific user location for over 48 hours with 10 mins time interval. 10^8 MC trials were performed independently every 10 mins, i.e., at each point in the figure, to assess the likelihood. Due to the convergence performance of the numerical integration using Monte Carlo method, outliers beyond the given requirement of 10^{-6} are inevitably involved (approximately 3% of cases over the duration in the example). If the average risk of false alarm over the given time interval is taken, the risk estimate could be biased to some extent due to such outliers. So, this investigation takes the median of probabilities over the given period such that the probability estimation can be robust against outliers from the numerical integration.

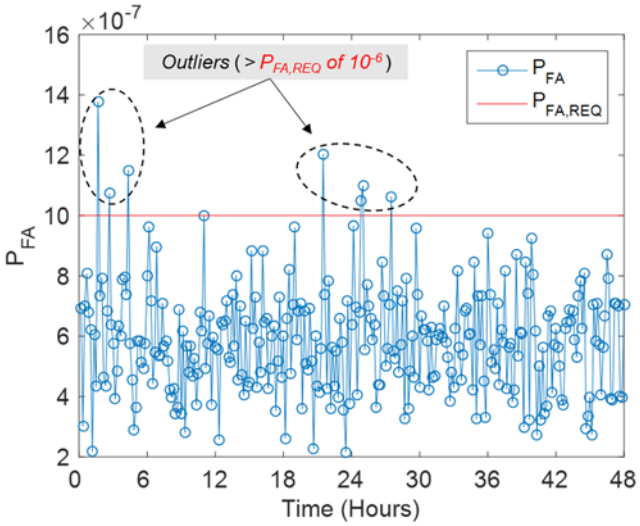

Fig. 5 Time series of the P_{FA} evaluated at a specific location over 48 hours. Outliers beyond the requirement (10^{-6}) within the circular dotted line

The first case assesses the P_{FA} of ARAIM integrity monitoring when only a single satellite failure is assumed. A simulation of a two day period is considered to account for the underlying computational uncertainty in the numerical method as well as various geometry conditions. In the simulation, the P_{FA} is estimated at each grid location and epoch. As described above, substantial outliers were observed due to the Monte Carlo method based computational error in all simulations performed. Hence, we take the median of the likelihood estimated over the simulation period (i.e., 48 hours) to obtain the robust measurement against possible outliers. Figure 6 shows the median of the P_{FA} obtained by applying a single satellite fault to the ARAIM fault monitoring algorithm. The maximum improvement is about 1% compared to the requirement of 10^{-6} (i.e., the minimum value is about 9 x 10^{-7}). Such improvement can be achieved in most regions, and it mainly comes from the valid number of orthogonal statistics in the transformed domain which are less than the number of the full ensemble of the statistics by at least five (i.e., the number of estimated states).

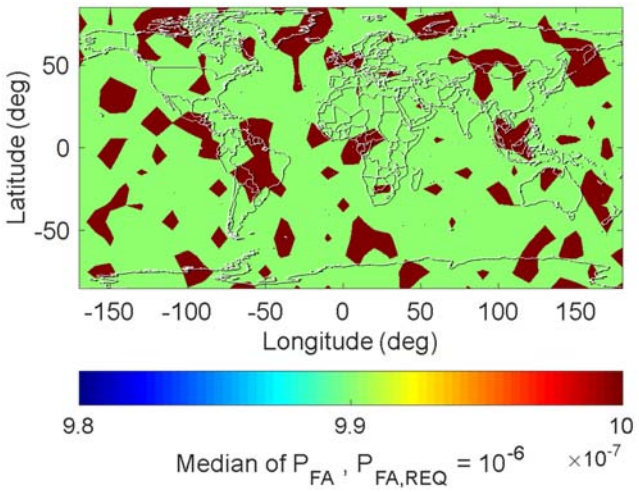

Fig. 6 Median P_{FA} obtained by considering single satellite failures and correlated ARAIM monitor test statistics.

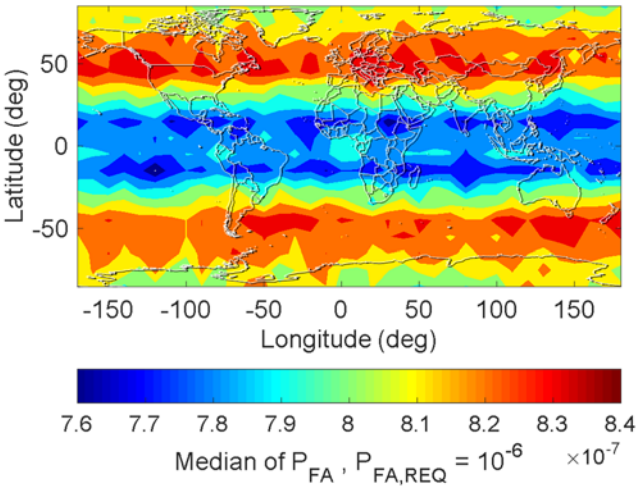

Fig. 7 Median of the P_{FA} of ARAIM fault monitoring when cross-correlations amongst test statistics are considered. Double satellite failures are applied to ARAIM FD algorithm

The P_{FA} for three other cases were obtained by assuming a pair of satellite failures and combined fault mode of a single and double satellite faults, and triple faults, respectively. As in the previous simulation in Figure 6, the same risk evaluation method and simulation parameters are used. Figure 7 shows the result when double satellite faults are applied to the ARAIM fault monitoring algorithm and the median P_{FA} is decreased down to approximately 76% of the requirement of 10^{-6}. As discussed in the single failure case, the predetermined continuity risk is allocated to more tests to determine the corresponding detection thresholds.

Thus, greater monitor thresholds are generated compared to the single fault case, resulting in improvement of the performance. However, the estimated probability is still quite close to the expected performance of 10^{-6}.

Next, the increased number of fault modes is considered in the FD test by applying both a single satellite fault and double failures in the same way as the previous simulations in Figures 6 and 7. Figure 8 represents the median value of P_{FA} when more fault modes are assumed. Since the greater number of fault hypotheses lead to reduced continuity risk allocation for each test, the minimum median value for the combined fault mode drops down to approximately 7 x $10^{-7,}$ which is about 8% improvement compared to that for the double fault case shown in Figure 7.

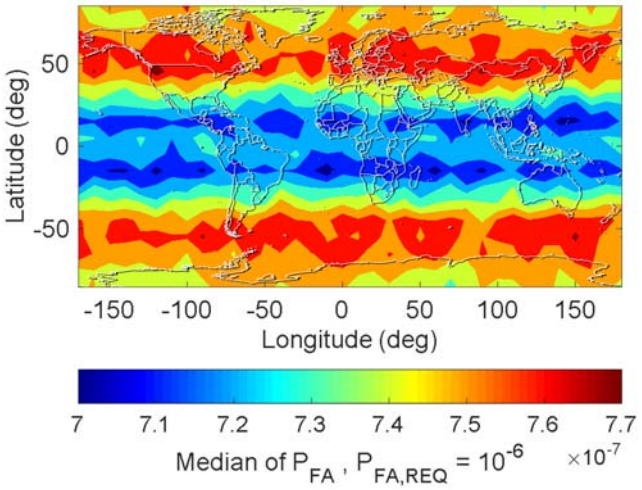

Fig. 8 Median of P_{FA} of ARAIM fault monitoring based on a combination of a single fault and a pair of failures

We also further investigated how the number of monitor test statistics (or the number of monitored fault modes) affects the ARAIM false alarm performance by applying the triple satellite fault hypothesis to ARAIM FD algorithm. Figure 9 shows the median P_{FA} when more fault modes are applied to the ARAIM algorithm. In this case, the lowest median value is decreased from approximately 7 x 10^{-7} for the combined fault mode case, shown in Figure 8, to roughly 5 x 10^{-7} for the triple fault mode (i.e., by about 28%). As expected, the false alarm performance of ARAIM fault monitoring improves due to the substantially increased number of fault modes. In this case, the reduction in the continuity budget allocated to each fault mode

is more dominant compared to the decrease in the effective amount of independent monitor statistics.

Since the actual P_{FA} tends to be less than the expected one, one can expect the implementation of a lower threshold to reduce the magnitude of HPL or VPL and therefore increase the fraction of the total time that the user's PL is less than a given alert limit. However, the impact of the reduced P_{FA} actual false alarm rate could be more complicated than such an argument would propose since the protection level is not a simple linear function of the detection threshold. The VPL equation employed in the baseline ARAIM user algorithm (Blanch et al., 2015) is as follows.

$$2Q\left(\frac{VPL - b^{(0)}}{\sigma^{(0)}}\right) + \sum_{k=1}^{N} P_{fault,k} Q\left(\frac{VPL - T_k - b^{(k)}}{\sigma^{(k)}}\right) = f(PHMI_{VERT/HOR}, P_{not\ monitored}) \quad (21)$$

Here $Q(\cdot)$ is the tail probability of a zero-mean unit normal distribution, $P_{fault,k}$, T_k and b_k are respectively the prior probability, detection threshold, and the magnitude of nominal bias for the k-th fault mode. The right hand side of the equation is a function of risk requirements: $PHMI_{VERT}$ and $PHMI_{HOR}$ are integrity risk requirements allocated to vertical and horizontal coordinate, respectively, and $P_{not\_monitored}$ is the allocation for fault modes that don't need to be monitored because their prior probabilities are too low compared to the risk requirement (Blanch et al., 2015). If we have a lower threshold here, the magnitude of VPL should get lower accordingly, such that the VPL equation holds for given integrity risk requirements.

In order to specify a change in VPL due to a change in the detection threshold, Table 2 shows two example calculations. The first column indicates the number of fault modes. With 24 GPS and 24 Galileo constellation, we observed approximately 10 to 15 fault modes on average in our simulations. Let us assume we set a lower threshold to take advantage of the margin in P_{FA}, i.e., half of 10^{-6} as shown in our findings. The second and third columns compare the K_{fa} in (6) for $P_{FA} = 10^{-6}$ to that for $P_{FA} = 0.5 * 10^{-6}$.

Table 2 Comparison of K_{fa} (P_{fa}=10^{-6}) and K_{fa} (P_{fa}=0.5×10^{-6})

No. of fault modes (h)	$P_{FA,REQ}$ in (6)		ΔK
	$P_{FA} = 10^{-6}$	$P_{FA} = 0.5 \times 10^{-6}$	
10	K_{fa}=5.3267	K_{fa}=5.4513	0.1246
15	K_{fa}=5.3999	K_{fa}=5.5230	0.1231

In these examples, the difference in K_{fa} is barely about 0.12, and such a difference would not be that significant in the computation of VPL in (21). Thus, although the minimum of median P_{FA} is decreased up to approximately 50% of the requirement of 10^{-6}, such improvement would not dramatically affect the magnitude of the protection level.

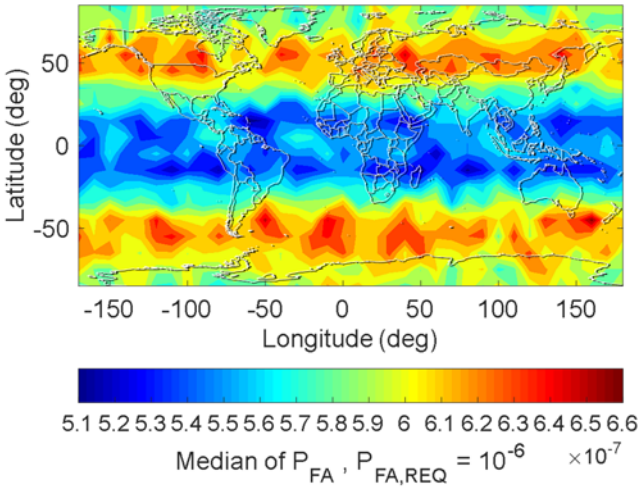

Fig. 9 Median of P_{FA} of ARAIM solution separation test when triple satellite faults are applied to the fault detection

The impact of the correlation between the solution separation monitors on the ARAIM false alarm rate is shown in this study. Also, it is demonstrated that the previously proposed assumption for the ARAIM continuity risk could not be over-conservative. However, the minimum P_{FA}, which is around half of the requirement might have been observed merely due to chance, because all possible multiple fault modes were not investigated in this investigation. Thus, more different types of satellite failures, including constellation faults,

need to be examined.

Conclusion

We conducted a preliminary assessment of the ARAIM false alarm risk by presenting a methodology to evaluate the actual risk based on the test correlation and applying the same ARAIM FD algorithm (Blanch et al. 2015; Joerger and Pervan 2016) to the risk evaluation. Using the proposed method and the baseline conditions, we have demonstrated how the cross-correlation amongst ARAIM test statistics affects the false alarm performance of ARAIM based integrity monitoring. We found that the maximum margin of approximately 30% of the predefined false alarm risk (e.g., 10^{-6}) was observed for the single plus double faults, and the maximum improvement of about 50% was achieved for the triple fault when the cross-correlation is accounted for. However, despite the approximately half as much improvement in the risk probability under the triple case, regarding the reduction of the magnitude of the horizontal or vertical protection level, the factor of two would not be substantial. Therefore, it was shown that the exact determination does not bring much benefit. This, as a result, is conclusive in verifying that the existing ARAIM implementation, such as the baseline FD algorithm and the continuity allocation (WG-C 2016; Blanch et al. 2015) appears to be not far from being optimal. Also, it is worth noting that the impact of the cross-correlation on the ARAIM false alarm risk might be more significant for multiple fault conditions such as constellation wide failure, but the marginal improvements in the protection bound imply no need of further investigation across a wide range of faults to achieve better performance. This understanding of the predicted system performance assessed from applying predefined design parameters and algorithms could be employed as a feasibility study especially during the initial phase of the ARAIM development and standardization (WG-C 2016) when the system design and the corresponding algorithm development will be carried out.

Most notably, this is the first work to the author's knowledge to investigate the cross-correlation effect of the ARAIM solution separation test on the actual ARAIM false alarm rate. Our results provide compelling evidence for the current continuity allocation and the ARAIM FD mechanism with a high level of accuracy and suggest that the current analysis seems to be more or less complete. However, it was found that the cross-correlation and temporal correlation of monitor statistics have opposing effects, as described in the previous related work (Pervan et al. 2017). Continuing research, therefore, will include the follow-up work designed

to evaluate the impact of temporal correlation between test statistics on ARAIM performance.

Acknowledgments

This work is conducted within the framework of a cooperation agreement between ENAC and DSNA/DTI for ENAC to provide scientific support to DTI on GNSS. The authors would like to thank the DSNA for their financial support of this work.

References

Bang E et al. (2018) ARAIM Test Statistic Correlation. Proc. ION ITM 2018, The Institute of Navigation, Reston, Virginia, January 2018, pp. 99-113

Bang E et al. (2019) Sample Temporal Correlation Effect on PHMI. Proc. ION ITM 2019, The Institute of Navigation, Reston, Virginia, USA, January 2019, pp. 85-99

Blanch J, Ene A, Walter T, Enge P (2007) An Optimized Multiple Hypothesis RAIM Algorithm for Vertical Guidance. Proc. ION GNSS 2007, The Institute of Navigation, Fort Worth, TX, USA, September 2007, pp. 2924-2933

Blanch J, Walter T, Enge P (2014) Exclusion for Advanced RAIM: Requirements and a Baseline Algorithm. Proc. ION ITM 2014, The Institute of Navigation, San Diego, California, USA, January 2014, pp. 99-107

Blanch J et al. (2015) Baseline Advanced RAIM User Algorithm and Possible Improvements. IEEE Transactions on Aerospace and Electronic Systems, 51(1):713–732

Federal Aviation Authority (2010) Phase II of the GNSS Evolutionary Architecture Study, FAA report. https://www.faa.gov/about/office_org/headquarters_offices/ato/service_units/techops/navservices/gnss/library/documents/media/GEASPhaseII_Final.pdf.

Genz A and Kwong K S (2000) Numerical Evaluation of Singular Multivariate Normal Distribution. Journal of Statistical Computation and Simulation, 68(1):1-21

Gene H G and Charles F V L (2013) Matrix Computations. 4th edition, The Johns Hopkins University Press, Baltimore, MD

Healy M J R (1968) Algorithm AS 6: Triangular Decomposition of a Symmetric Matrix. Journal of the Royal Statistical Society. Series C (Applied Statistics), 17(2):195-197

ICAO (2014) Annex 10, Aeronautical Telecommunications, Volume 1 (Radio Navigation Aids), Amendment 89

Joerger M and Pervan B (2016) Fault Detection and Exclusion Using Solution Separation and Chi-Squared ARAIM. IEEE Transactions on Aerospace and Electronic Systems, 52(2):726-742

Kelly R J (1998) The Linear Model, RNP, and the Near-Optimum Fault Detection and Exclusion Algorithms. Global Positioning System: Papers Published in Navigation, Journal of The Institute of Navigation, 5:227-259

Lee Y C (1986) Analysis of range and position comparison methods as a means to provide GPS integrity in the user receiver. Proc. the 42nd Annual Meeting. The Institute of Navigation, Seattle, Washington, USA, June 1986, pp. 1-4

Lee Y C and McLaughlin M P (2007) Feasibility Analysis of RAIM to Provide LPV-200 Approaches with Future GPS. Proc. ION GNSS 2007, The Institute of Navigation, Fort Worth, TX, USA, September 2007, pp. 2898-2910

Milner C et al. (2017) Methods of Integrity Risk Computation for ARAIM FDE. Proc. ION GNSS+ 2017, The Institute of Navigation, Portland, Oregon, USA, September 2017, pp. 2371-2387

Parkinson B W and Axelrad P (1998) Autonomous GPS integrity monitoring using the pseudorange residual. Navigation, 35(2):255-274

Pervan B, Khanafseh S, Patel J (2017) Test Statistic Auto- and Cross-correlation Effects on Monitor False Alert and Missed Detection Probabilities. Proc. ION ITM 2017, The Institute of Navigation, Monterey, California, USA, January 2017, pp. 562-590

RTCA Special Committee 159 (1991) Minimum Operational Performance Standards (MOPS) for Airborne Supplemental Navigation Equipment Using Global Positioning System (GPS). RTCA Document No. DO-208

Sturza M A (1988) Navigation System Integrity Monitoring Using Redundant Measurements. Navigation, 35(4):483-501

Working Group C (WG-C) (2016) ARAIM Technical Subgroup Milestone 3 Report. http://www.gps.gov/policy/cooperation/europe/2016/working-group-c/ARAIM-milestone-3-report.pdf.

Young R S Y and McGraw G A (2003) Fault Detection and Exclusion Using Normalized Solution Separation and Residual Monitoring Methods. Navigation, 50(3):151-170

Zhai Y, Joerger M, Pervan B (2015) Continuity and Availability in Dual-Frequency Multi-Constellation ARAIM. Proc. ION GNSS+ 2015, The Institute of Navigation, Tampa, Florida, USA, September 2015, pp. 664-674

Zhai Y, Joerger M, Pervan B (2018) Fault Exclusion in Multi-Constellation Global Navigation Satellite Systems. The Journal of Navigation, 71(6):1281-1298

Zhai Y, Pervan B, Joerger M (2016) H-ARAIM Exclusion: Requirements and Performance. Proc. ION GNSS+ 2016, The Institute of Navigation, Portland, Oregon, USA, September 2016, pp. 1713-1725

Appendix

This section gives some elements for the development of (13) and (15). The derivation of the equations is based on the method in Genz and Kwong (2000). First, the reduction of the integration dimension is discussed. In (12), the integration region is represented as $-\mathbf{T} < \mathbf{Qy} = \mathbf{Q}[y_1, y_2, \cdots, y_h]^{\boldsymbol{T}} < \mathbf{T}$, and the matrix $\mathbf{Q}$ has the lower triangular form whose elements $q_{ij} = 0$ for all $j > r$. Here let us assume that a rearrangement of the inequalities has been completed such that the matrix $\mathbf{Q}$ has the following form:

$$\mathbf{Q} = [\mathbf{Q}'_{h\times r}\ 0_{h\times h-r}]$$

$$= \begin{bmatrix} q_{1,1} & 0 & 0 & \cdots & \cdots & 0 & \cdots & 0 \\ \vdots & \vdots & \vdots & \vdots & \vdots & \vdots & \vdots & \vdots \\ q_{k_1,1} & 0 & 0 & \cdots & \cdots & 0 & \cdots & 0 \\ * & q_{1,2} & 0 & \cdots & \cdots & 0 & \cdots & 0 \\ \vdots & \vdots & \vdots & \vdots & \vdots & \vdots & \vdots & \vdots \\ * & q_{k_2,2} & 0 & \cdots & \cdots & 0 & \cdots & 0 \\ \vdots & \ddots & \ddots & \ddots & \ddots & 0 & \cdots & 0 \\ * & * & \cdots & * & q_{1,r} & 0 & \cdots & 0 \\ \vdots & \vdots & \vdots & \vdots & \vdots & \vdots & \vdots & \vdots \\ * & * & \cdots & * & q_{k_r,r} & 0 & \cdots & 0 \end{bmatrix}$$

k_1 constraints for y_1

k_2 constraints for y_2

Fig. 10 Transformation matrix

where $\mathbf{Q}'$ is a h x r submatrix of $\mathbf{Q}$ with permuted columns in terms of y_i for $i = 1, \cdots, r$, and

the subscription k_i for $i = 1, \cdots, r$ denotes the number of inequalities in each group of y_i (i.e., $\sum_{j=1}^{r} k_j = h$). Only $y_1, y_2, \cdots, y_{\mathrm{r}}$ variables have constraints whilst the remaining h - r variables $y_{\mathrm{r+1}}, y_{\mathrm{r+2}}, \cdots, y_{\mathrm{h}}$ are not constrained, so integrations in (12) which are related to those unconstrained variables should be all equal to 1 and those terms thus are not included in the equation. Therefore, the integration is reduced to r dimensional one in (13).

Next, normalization can be performed such that the matrix $\mathbf{Q}$ has the form in (22) where entries corresponding to each group of y_i (e.g., $q_{1,2}, \cdots, q_{k_2,2}$ for y_2 in the light blue colored box in Figure 10) are all ones and $*$ could be a zero or nonzero component. In the process, if an inequality needs to be divided by a negative number, the order of the inequality must be changed so that after division by a negative number, a scaled lower limit becomes an upper limit, and a scaled upper limit becomes a lower limit.

$$\overline{\mathbf{Q}} = [\overline{\mathbf{Q}}'_{h\times r}\ \mathbf{0}_{h\times h-r}] = \begin{bmatrix} 1_{1,1} & 0 & 0 & \cdots & \cdots & 0 & \cdots & 0 \\ \vdots & \vdots & \vdots & \vdots & \vdots & \vdots & \vdots & \vdots \\ 1_{k_1,1} & 0 & 0 & \cdots & \cdots & 0 & \cdots & 0 \\ * & 1_{1,2} & 0 & \cdots & \cdots & 0 & \cdots & 0 \\ \vdots & \vdots & \vdots & \vdots & \vdots & \vdots & \vdots & \vdots \\ * & 1_{k_2,2} & 0 & \cdots & \cdots & 0 & \cdots & 0 \\ \vdots & \ddots & \ddots & \ddots & \ddots & 0 & \cdots & 0 \\ * & * & \cdots & * & 1_{1,r} & 0 & \cdots & 0 \\ \vdots & \vdots & \vdots & \vdots & \vdots & \vdots & \vdots & \vdots \\ * & * & \cdots & * & 1_{k_r,r} & 0 & \cdots & 0 \end{bmatrix} \tag{22}$$

L and **U** designate the new limit vectors after permutations, normalizations, and interchanges of the original limit vectors -**T** and **T** (see (13)), such that the new set of constraints for the integration region takes the following form:

$$\mathbf{L} < \overline{\mathbf{Q}}'\mathbf{y} = \overline{\mathbf{Q}}'^{[y_1, y_2, \cdots, y_r]^T} < \mathbf{U} \tag{23}$$

We can now produce explicit expressions for the limits of the continuous integration variables. For instance, let $m_i = \sum_{j=1}^{i} k_j$, then the revised limits for y_i in (23) can be determined by k_i constraints for y_i as shown in (24) and (25). Here n is the index for the row of the matrix $\overline{\mathbf{Q}}'$.

$$L_i(y_1, y_2, \cdots, y_{i-1}) = \max_{m_{i-1} < n \le m_i} \left(l_n - \sum_{j=1}^{i-1} q_{n,j} y_j \right) \tag{24}$$

$$U_i(y_1, y_2, \cdots, y_{i-1}) = \min_{m_{i-1} < n \le m_i} \left(u_n - \sum_{j=1}^{i-1} q_{n,j} y_j \right) \tag{25}$$

By applying these bounds, the resulting expression of the integration in (12) becomes the expression in (13).

Second, the form of integration in (13) is further simplified using the transformation in (26), such that standard numerical integration methods are easily applied to the evaluation of the probability.

$$z_\mathrm{i} = F(y_i) \quad \text{for } i = 1, \cdots, r \tag{26}$$

$F(\cdot)$ designates the Gaussian cumulative distribution function (CDF). By definition, $\phi(y_i) dy_i = dz_i$ where ϕ indicates the Gaussian probability density function (PDF) and (13) becomes

$$\int_{\bar{L}_1}^{\bar{U}_1} \int_{\bar{L}_2}^{\bar{U}_2(z_1)} \cdots \int_{\bar{L}_r(z_1, z_2, \cdots, z_{r-1})}^{\bar{U}_r(z_1, z_2, \cdots, z_{r-1})} d\boldsymbol{z} \tag{27}$$

where new limits for z_i, $\bar{L}$ and $\bar{U}$ are derived based on (26).

$$\bar{L}_i(z_1, \cdots, z_{i-1}) = F\left(L_i\left(F^{-1}(z_1), \cdots, F^{-1}(z_{i-1}) \right) \right) \tag{28}$$

$$\bar{U}_i(z_1, \cdots, z_{i-1}) = F\left(U_i\left(F^{-1}(z_1), \cdots, F^{-1}(z_{i-1}) \right) \right) \tag{29}$$

Lastly, let us put $z_\mathrm{i} = \bar{L}_i + (\bar{U}_i - \bar{L}_i) u_i$ for $i = 1, \cdots, r$ so that integration limits all have an interval $[0,1]$. From $dz_i = (\bar{U}_i - \bar{L}_i) du_i$, equation (27) can be expressed in the form of (14) in the previous section**:**

$$(\bar{U}_1 - \bar{L}_1)\int_0^1 \left(\bar{U}_2(u_1) - \bar{L}_2(u_1)\right)\cdots\int_0^1 \left(\bar{U}_r(u_1,\cdots,u_{r-1}) - \bar{L}_r(u_1,\cdots,u_{r-1})\right)\int_0^1 d\boldsymbol{u} \quad (30)$$

Author Biographies

Eugene Bang received his Ph.D. degree in Aerospace Engineering from Korea Advanced Institute of Science and Technology (KAIST), Republic of Korea, in 2017. He currently works as a postdoctoral research associate at Ecole Nationale de l'Aviation Civile (ENAC) in Toulouse, France. His areas of interest include high integrity applications of GNSS and advanced receiver autonomous integrity monitoring (ARAIM).

Carl Milner is an Assistant Professor within the Telecom Lab at the Ecole Nationale de l'Aviation Civile. He has a master's degree in mathematics from the University of Warwick, a Ph.D. in Geomatics from Imperial College London and has completed the graduate trainee program at the European Space Agency. His research interests include GNSS augmentation systems, integrity monitoring, air navigation and applied mathematics.

Christophe Macabiau graduated as electronics engineer in 1992 from the ENAC (Ecole Nationale de l'Aviation Civile) in Toulouse, France. Since 1994, he has been working on the application of satellite navigation techniques to civil aviation. He received his Ph.D. in 1997 and has been in charge of the signal processing lab of ENAC since 2000, where he also started dealing with navigation techniques for terrestrial navigation. He is currently the head of the TELECOM team of ENAC, which includes research groups on signal processing and navigation, electromagnetics, and data communication networks.